Action Potential Initiation in Auditory Nerve Fibers via Cochlear Implant Stimulation is Dependent on Ion Channel Population and Electrode Location

Jason Boulet[1,2] **and Ian Bruce**[1,2,3]

Auditory Engineering Laboratory[1], McMaster Integrative Neuroscience Discovery & Study[2],
Department of Electrical & Computer Engineering, McMaster University[3], Hamilton, ON, Canada

Abstract

Numerous findings indicate that auditory nerve fibers (ANFs) of deafened cats presented with high rates of electrical stimulation, given by cochlear implants, undergo spike-rate adaptation and accommodation. A simulation study by Negm and Bruce (2008) reported that low-threshold potassium (KLT) and hyperpolarization-activated cyclic nucleotide-gated cation (HCN) channels are the determining components of this behavior, whereas standard Hodgkin–Huxley-type ANF models, containing fast Nav and delayed-rectifier Kv channels only, cannot explain adaptation.

To investigate the effects of the spatial distribution of multiple ion channels species on the neural response, we carry out a compartmental simulation study of the electrical stimulation of a type I feline ANF. We base our neuron morphology on Woo et al. (2010) and implement two versions of the model: A) just fast Nav and delayed-rectifier Kv at all nodes of Ranvier and B) with the addition of KLT & HCN channels (Yi et al., 2010) at the first peripheral node and on the nodes of Ranvier neighboring the soma. Our results indicate that stimulation of peripheral nodes in model B exhibits a higher threshold current for action potential generation, shorter mean latency and smaller jitter than for model A. This effect is observed even at peripheral nodes in model B that do not themselves have the KLT & HCN channels but are adjacent to nodes that do. In contrast, the statistics of action potential generation are identical between the two model versions for stimulation at central nodes of Ranvier. The properties of refractoriness, spike-rate adaptation and accommodation for the two model versions will be explored and discussed.

This research was supported by the Natural Sciences and Engineering Research Council of Canada (Discovery Grant #261736).

I. INTRODUCTION

- Recent studies have shown that electrically stimulated type I cat ANFs display behavior such as spike-rate adaptation and accommodation (Zhang et al., 2007).
- Computational models of the ANF that are based on the Hodgkin–Huxley equations containing only Nav and Kv channels do not adequately describe spike-rate adaptation and accommodation.
- Yi et al. (2010) have experimentally found HCN channels at the first peripheral node (or terminal) and the nodes neighboring the soma in mouse spiral ganglion cells. KLT channels are known to co-localize with HCN channels.
- A computational membrane-node model of the cat ANF incorporating Nav, Kv, KLT and HCN channels has shown that spike-rate adaptation increases with the rate of electrical stimulation (Negm and Bruce, 2008).
- We built a compartmental model of the cat ANF in an effort to better understand how responses depend on the location and populations of voltage-gated ion channel species (Nav, Kv, KLT and HCN) and the location and rate of electrical stimulation from a CI.
- The morphology of the compartmental model is derived from Woo et al. (2010).
- In order to simulate the activity of various ion channels species, we employ a stochastic characterization since the ensuing fluctuations about the threshold are considered important to users of cochlear implants (Bruce et al., 1999a,b).

II. METHODS: Ion Channel Particle Activation/Inactivation

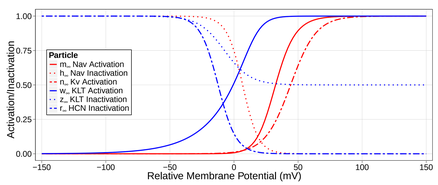

Figure 1: The steady-state activation/inactivation functions at 37°C. We adjusted w_∞, z_∞ and r_∞ from 22°C (Rothman and Manis, 2003) to 37°C (Cartee, 2000).

II. METHODS: ANF Models

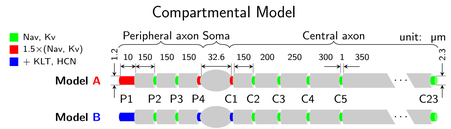

Figure 2: Hossain et al. (2005) found high densities of Nav1.6 channels located at P1, P4 and C1 in the mouse ANF. Yi et al. (2010) have shown the presence of HCN channels at the same nodes in mouse spiral ganglion cells. KLT channels are known to co-localize with HCN channels. We base the morphology of the feline ANF on Woo et al. (2010). Note that the soma is myelinated, which contrasts with those of the mouse and human ANF.

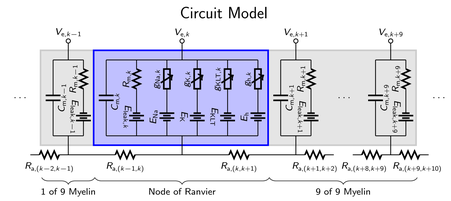

Figure 3: The circuit model is solved using a partial differential equation (PDE) and is discretized using the Crank–Nicholson scheme found in Mino et al. (2004). In the above diagram, k refers to the compartment number, V_k is the extracellular potential, R_a is the axial resistance, R_m is the membrane resistance, C_m is the membrane capacitance, E_i and g_i are the channel reversal potentials and conductances, respectively. The leakage reversal potential, E_{leak}, is uniquely set at each compartment to produce a fixed resting potential of -78 mV.

II. METHODS: Electrical Stimulation

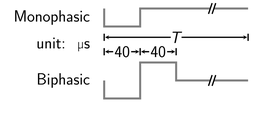

We stimulated the ANF with extracellular current injection. The stimulating electrode is a spherical monopole with radius 1 µm (Mino et al., 2004), positioned 500 µm above the desired site of stimulation (nodes P1 to C5). Monophasic cathodic pulses have a duration of 40 µs whereas biphasic pulses are constructed from 40 µs each of cathodic and immediately-following anodic stimulation. Propagating action potentials were detected by measuring the membrane potential at node C17.

II. METHODS: Ion Channel Simulation

Channel kinetics obey continuous-time discrete-state Markov processes. The state transition diagrams for Nav, Kv (Mino et al., 2002), KLT and HCN (Negm and Bruce, 2008) are given by

$$m_0 h_0 \underset{\beta_m}{\overset{3\alpha_m}{\rightleftharpoons}} m_1 h_0 \underset{2\beta_m}{\overset{2\alpha_m}{\rightleftharpoons}} m_2 h_0 \underset{3\beta_m}{\overset{\alpha_m}{\rightleftharpoons}} m_3 h_0$$
$$\alpha_h \downarrow \uparrow \beta_h \qquad \alpha_h \downarrow \uparrow \beta_h \qquad \alpha_h \downarrow \uparrow \beta_h \qquad \alpha_h \downarrow \uparrow \beta_h , \tag{1}$$
$$m_0 h_1 \underset{\beta_m}{\overset{3\alpha_m}{\rightleftharpoons}} m_1 h_1 \underset{2\beta_m}{\overset{2\alpha_m}{\rightleftharpoons}} m_2 h_1 \underset{3\beta_m}{\overset{\alpha_m}{\rightleftharpoons}} m_3 h_1$$

$$n_0 \underset{\beta_n}{\overset{4\alpha_n}{\rightleftharpoons}} n_1 \underset{2\beta_n}{\overset{3\alpha_n}{\rightleftharpoons}} n_2 \underset{3\beta_n}{\overset{2\alpha_n}{\rightleftharpoons}} n_3 \underset{4\beta_n}{\overset{\alpha_n}{\rightleftharpoons}} n_4 , \tag{2}$$

$$w_0 z_0 \underset{\beta_w}{\overset{4\alpha_w}{\rightleftharpoons}} w_1 z_0 \underset{2\beta_w}{\overset{3\alpha_w}{\rightleftharpoons}} w_2 z_0 \underset{3\beta_w}{\overset{2\alpha_w}{\rightleftharpoons}} w_3 z_0 \underset{4\beta_w}{\overset{\alpha_w}{\rightleftharpoons}} w_4 z_0$$
$$\alpha_z \downarrow \uparrow \beta_z \qquad \alpha_z \downarrow \uparrow \beta_z \qquad \alpha_z \downarrow \uparrow \beta_z \qquad \alpha_z \downarrow \uparrow \beta_z , \tag{3}$$
$$w_0 z_1 \underset{\beta_w}{\overset{4\alpha_w}{\rightleftharpoons}} w_1 z_1 \underset{2\beta_w}{\overset{3\alpha_w}{\rightleftharpoons}} w_2 z_1 \underset{3\beta_w}{\overset{2\alpha_w}{\rightleftharpoons}} w_3 z_1 \underset{4\beta_w}{\overset{\alpha_w}{\rightleftharpoons}} w_4 z_1$$

$$r_0 \underset{\beta_r}{\overset{\alpha_r}{\rightleftharpoons}} r_1 \tag{4}$$

where the colored states indicate those which are fully open and hence contribute to conducting ionic current. We simulate the 4 voltage-gated ion channel types with a channel number tracking (CNT) algorithm (Chow and White, 1996; Mino et al., 2002).

III. RESULTS: Action Potential Initiation

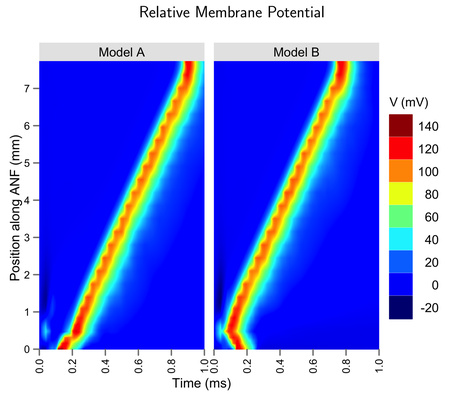

Figure 4: One example of a simulation of the relative membrane potential as a function of time and position along the ANF. The position of peripheral node 1 (P1) is at 0 mm. In this particular trial, we present the ANF with a biphasic stimulus over P4.

III. RESULTS: Monophasic Single-Pulse Statistics

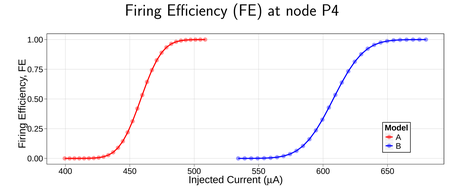

Figure 5: FE is defined as the probability of an action potential occurring upon the delivery of a single pulse of current to an ANF. Data points are the mean values from 1000 Monte-Carlo trials and are fit to an integrated Gaussian (Bruce et al., 1999a). The threshold current θ is the current at FE = 0.5 and the relative spread is RS = $\frac{\sigma}{\theta}$. Model B has a greater θ than model A.

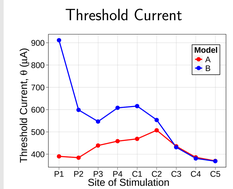

Figure 6: Threshold current (θ) across all nodes. Error bars give the 95% confidence intervals of the fit to the 1000 trials.

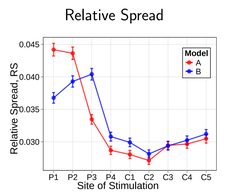

Figure 7: Relative Spread (RS) across all nodes. Error bars give the 95% confidence intervals of the fit to the 1000 trials.

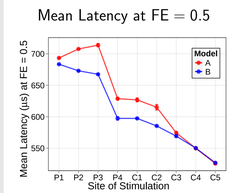

Figure 8: Mean Latency (ML) estimated at FE = 0.5. Error bars show ± 1 standard error of the mean from the 1000 trials.

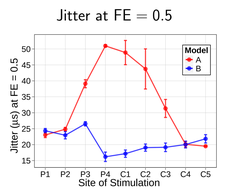

Figure 9: Jitter (JT) estimated at FE = 0.5. Error bars show ± 1 standard error of the mean from the 1000 trials.

III. RESULTS: Spike-Rate Adaptation

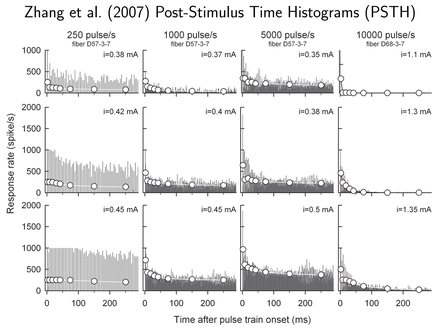

Figure 10: Examples of spike-rate adaptation seen in the PSTHs from the responses of one cat ANF at the stimulus rates of 250, 1000, and 5000 pulses/s, whereas a second ANF provided the 10,000 pulses/s rate data. Each column contains PSTHs obtained at three stimulus levels. The bars have a resolution of 1 ms, whereas the open circles and lines represent bins of increasing duration: (0, 4], (4, 12], (12, 24], (24, 36], (36, 48], (48, 100] and (100, 300] ms intervals. Reproduced with permission from Zhang et al. (2007).

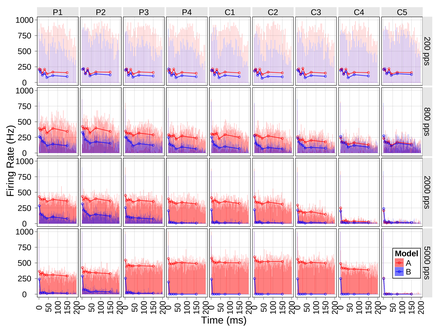

Figure 11: PSTHs for our model ANFs. The responses are shown for stimulated nodes P1 to C5 at the stimulus rates 200, 800, 2000 and 5000 pulses/s. The PSTHs were generated by averaging across 50 Monte-Carlo simulations of 200 ms for two sets of time-bins. The same plotting convention is used as in Fig. 10.

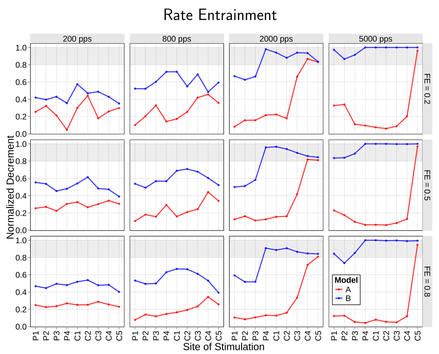

Figure 12: Rate decrement is defined by the mean rate in the onset window (0, 12] ms subtracted by the mean rate in the final window (100, 200] ms. The normalized decrement is just the rate decrement divided by the onset rate (Zhang et al., 2007). Strong adaptation is indicated by the gray region [0.8, 1.0].

IV. CONCLUSIONS

- Greater threshold currents in model B than model A, but only in the proximity of KLT and HCN channels
- At the nodes neighboring the myelinated soma, HCN and KLT channels seem to exert 1) a regularizing effect on spike timing and 2) a shorter mean latency
- Model B shows signs of accommodation behaviour at 2000 and 5000 pulses/s
- Model A displays evidence of facilitation for high stimulus rates of 2000 and 5000 pulses/s, similarly to Heffer et al. (2010) in guinea pig ANF
- There is a complex, but clear interaction across all outcome measures: between model (ion channel population) and electrode placement (initially activated node)
- Further studies must be done to address the mechanisms of accommodation and facilitation, taking into account the dependence on location and model. Both passive and active properties will be investigated.

References

Bruce, I. C., White, M. W., Irlicht, L. S., O'Leary, S. J., and Clark, G. M. (1999a). The effects of stochastic neural activity in a model predicting intensity perception with cochlear implants: low-rate stimulation. *IEEE Transactions on Biomedical Engineering*, 46(12):1393–1404.

Bruce, I. C., White, M. W., Irlicht, L. S., O'Leary, S. J., Dynes, S., Javel, E., and Clark, G. M. (1999b). A stochastic model of the electrically stimulated auditory nerve: single-pulse response. *IEEE Transactions on Biomedical Engineering*, 46(6):617–629.

Cartee, L. A. (2000). Evaluation of a model of the cochlear neural membrane. II: Comparison of model and physiological measures of membrane properties measured in response to intrameatal electrical stimulation. *Hearing Research*, 146(1-2):153–166.

Chow, C. and White, J. A. (1996). Spontaneous action potentials due to channel fluctuations. *Biophysical Journal*, 71:3013–3021.

Heffer, L. F., Sly, D. J., Fallon, J. B., White, M. W., Shepherd, R. K., and O'Leary, S. J. (2010). Examining the auditory nerve fiber response to high rate cochlear implant stimulation: chronic sensorineural hearing loss and facilitation. *Journal of Neurophysiology*, 104(6):3124–3135.

Hossain, W. A., Antic, S. D., Yang, Y., Rasband, M. N., and Morest, D. K. (2005). Where is the spike generator of the cochlear nerve? Voltage-gated sodium channels in the mouse cochlea. *Journal of Neuroscience*, 25(29):6857–6868.

Mino, H., Rubinstein, J. T., Miller, C. A., and Abbas, P. J. (2004). Effects of electrode-to-fiber distance on temporal neural response with electrical stimulation. *IEEE Transactions on Biomedical Engineering*, 51(1):13–20.

Mino, H., Rubinstein, J. T., and White, J. A. (2002). Comparison of algorithms for the simulation of action potentials with stochastic sodium channels. *Annals of Biomedical Engineering*, 30(4):578–587.

Negm, M. H. and Bruce, I. C. (2008). Effects of I_h and I_{KLT} on the response of the auditory nerve to electrical stimulation in a stochastic Hodgkin-Huxley model. *Annual International Conference of the IEEE Engineering in Medicine and Biology Society*, 2008:5539–5542.

Rothman, J. S. and Manis, P. B. (2003). The roles potassium currents play in regulating the electrical activity of ventral cochlear nucleus neurons. *Journal of Neurophysiology*, 89(6):3097–3113.

Woo, J., Miller, C. A., and Abbas, P. J. (2010). The dependence of auditory nerve rate adaptation on electric stimulus parameters, electrode position, and fiber diameter: a computer model study. *Journal of the Association for Research in Otolaryngology*, 11(2):283–296.

Yi, E., Roux, I., and Glowatzki, E. (2010). Dendritic HCN channels shape excitatory postsynaptic potentials at the inner hair cell afferent synapse in the mammalian cochlea. *Journal of Neurophysiology*, 103(5):2532–2543.

Zhang, F., Miller, C. A., Robinson, B. K., Abbas, P. J., and Hu, N. (2007). Changes across time in spike rate and spike amplitude of auditory nerve fibers stimulated by electric pulse trains. *Journal of the Association for Research in Otolaryngology*, 8(3):356–372.

bouletjw@mcmaster.ca